

THE VULTURE SURVEY II: ANALYZING THE EVOLUTION OF CIV ABSORBERS

NIGEL L. MATHES, CHRISTOPHER W. CHURCHILL¹ AND MICHAEL T. MURPHY²

¹*New Mexico State University, Las Cruces, NM 88003*

²*Centre for Astrophysics and Supercomputing, Swinburne University of Technology, Victoria 3122, Australia*

ABSTRACT

We present the second part of The Vulture Survey with the goal of measuring the evolutionary properties of CIV absorbers from $1 < z < 5$. We measure the equivalent widths and apparent optical depth column densities of HELLA individual systems in the spectra of LESS HELLA individual quasar lines of sight to derive the number of absorbers per comoving path length, the equivalent width and column density frequency distributions, and the cosmic mass fraction in CIV. We compare to prior surveys and to trends in the evolution of galaxies, the cosmic ultraviolet background, and cosmic metallicity. We also probe a previously unsurveyed population of weak CIV absorbers, showing that these systems evolve passively with redshift, not partaking in the cycle of baryons into and out of galaxy halos.

Keywords: galaxies: halos — quasars: absorption lines

1. INTRODUCTION

One of the most elusive yet important goals in extragalactic research aims to discover how galaxies form, grow, and evolve in an effort to truly understand our place in the universe. The creation of a galaxy begins with a cosmic overdensity, where matter congregates to begin the process of building complex structures of stars, gas, and dust. Feedback from star formation and AGN, along with mergers, shape the galaxy and its surroundings into complex environments. The stage of most uncertainty throughout this process involves feedback, the injection of energy into the gaseous medium within and outside of galaxies which, as has been shown in simulations, is required to produce realistic looking galaxies.

The details of this complex process should be observable in the relationship between the stars in the galaxy and the gas phase material located between the stars within the galaxy (interstellar medium; ISM), just outside the galaxy (circumgalactic medium; CGM), and between galaxies themselves (intergalactic medium; IGM). Unfortunately, detailed observations of this gas are difficult as it remains mostly neutral (CITATION), and therefore does not strongly emit. Therefore, massive efforts have been undertaken to observe this gas in absorption using the most advanced telescopes.

CIV absorption lines are some of the better tracers of metal enriched gas around galaxies across cosmic time due to their existence in a wide range of astrophysical conditions, and their ease of observation with optical, ground-based telescopes. Specifically, the CIV $\lambda\lambda 1548, 1550$ doublet traces gas around galaxies with ionization parameters from $SOMETHING < \log U < SOMETHINGELSE$, and from redshifts $1 < z < 5$ in optical spectra. These absorbers have high oscillator strengths and trace an abundant metal, allowing for detections even in low metallicity gas with sufficiently high signal-to-noise spectra, making them ideal for inventorying a large portion of the CGM and IGM.

Beginning history of things here:

The first study to characterize intervening CIV absorbers was /citeYoung1982, which determined that these lines were randomly distributed in redshift in a manner consistent with absorption from intervening galaxies. /citeSargent1988 also showed that the number density of systems per unit redshift decreases with increasing redshift from $1.8/le z_{em}/le 3.56$. /citeSteidel1990, examining strong CIV absorbers at redshifts between $1.3/le z_{abs}/le 4.0$, found also that the number of CIV absorption systems per unit redshift range decreases with increasing redshift, in a manner inconsis-

tent with a constant comoving density of absorbers. Therefore, they stated, the properties of CIV absorbers must evolve over time.

In terms of kinematics, /citeSteidel1990 noted that the peak in the CIV two-point correlation function on velocity scales $200/le \Delta v/le 600 \text{ km s}^{-1}$ appears to have the same power at low and high redshift. /citeRauch1996 examined the velocity structure of intervening CIV absorbers in the spectra of 3 intermediate redshift quasars and determined that gas temperatures were likely near $3.8/imes 10^4 \text{ K}$, and the TPCF of CIV systems suggests that there is more than one source of velocity dispersion. They interpret the shape of the resulting TPCF as owing to ensembles of objects with the kinematics of dwarf galaxies on a small scale, while following the Hubble flow on a larger scale.

Churchill et al. (1999) examined data from the Hubble Space Telescope Faint Object Spectrograph for CIV absorbers associated with known MgII absorbers measured in high resolution Keck/HIRES data. They noticed a strong correlation between MgII kinematics and CIV equivalent width. They interpreted that this correlation could imply a connection between outflowing MgII clouds and higher ionization state halo gas.

? measured the kinematics and column density differences of CIV absorption systems along the lines of sight to three gravitationally lensed quasars. They found the spatial distribution of the gas to be mostly featureless with detectable velocity shear up to $\sim 70 \text{ kms}$. They found the clouds quiescent, in that the energy transmitted to the gas as measured by the amount of turbulence derived along the line of sight, and therefore determined that the absorbing structures are not internal to galaxies. They posited that CIV absorbers could be gas expelled recently or pre-enriched from earlier star formation.

Chen et al. (2001) examined 14 galaxy absorber pairs, along with 36 galaxies without associated CIV absorption lines. They found that CIV absorption line systems cluster strongly on velocity scales of $v \lesssim 250 \text{ km s}^{-1}$ and impact parameter scales of $\rho \lesssim 100 h^{-1} \text{ kpc}$. In addition, they note that galaxies of all morphological types and luminosities can possess extended gaseous envelopes, with covering factors near unity, at impact parameters less than 100 kpc. They concluded that accreting satellites are the most likely sources of this metal enriched halo gas.

?, ?, and ? all measured the comoving number of CIV absorbers per redshift path length in the spectra of background quasars. Together, they find that, when considering CIV absorbers with equivalent widths greater than $W_r^{1548} > 0.3 \text{ \AA}$, the number of absorption doublets

per unit redshift decreases with increasing redshift for $1.2 < z < 4.5$.

? directly measured the metallicity distribution function for the $z \sim 2.5$ intergalactic medium in the spectra of seven quasars. They found no evidence for a universal metallicity floor, as had been suggested for some scenarios of Population III enrichment in the early universe. In addition, they found no trends in metallicity as a function of IGM density.

? used a novel method of identifying pseudoclouds in C IV $\lambda\lambda 1548, 1550$ systems and measuring their individual properties with the pixel optical depth method. She generated the C IV column density distribution, and calculated from it the cosmic mass density of C IV absorbers (Ω_{CIV}) from $2 < z < 5$. She found a lack of redshift evolution in (Ω_{CIV}) for absorbers of all column densities, with (Ω_{CIV}) $\simeq 5 \times 10^{-8}$ at $z = 2$ and (Ω_{CIV}) $\simeq 2 \times 10^{-8}$ at $z = 5$.

In the following paper in this series, ? attempted to identify C IV systems associated with galactic outflows. By analyzing velocity widths, she found that roughly half of the systems with $\tau(\text{CIV}) > 0.4$ have widths consistent with outflowing winds. She concluded, after accounting for ionization from galaxy-like spectra and AGN, that almost all lower column density systems and roughly half of high column density C IV systems lie in the iGM, while half of the highest column density systems could be the direct result of outflows ionized by their parent galaxies.

? analyzed a single high equivalent width C IV system at $z_{\text{abs}} = 5.7238$, reporting that neither the column density distribution nor its integral evolves significantly from 1 to 4.5 Gyr after the big bang. This high redshift detection implies that either a large fraction of intergalactic metals were in place even at high redshift, or that this high column density system has origins in a highly ionized outflow.

? studied 63 damped Lyman- α (DLA) systems and 11 sub-DLAs with associated C IV absorption. They detected C IV clouds moving at velocities in excess of the escape speed, determined by measuring the total line width of the neutral gas profile, in roughly 40% of their systems. They inferred that these clouds may arise in high ionized outflowing winds, powered by galaxies with star formation rates (SFR) of $\sim 2 M_{\odot} \text{ yr}^{-1}$.

? surveyed 49 low redshift quasars with high resolution *Hubble Space Telescope* ultraviolet (UV) spectra for $z < 1$ C IV candidates. They were able to measure dN/dX , finding that it has not significantly evolved since $z = 5$. They also constructed the column density frequency distribution, fitting it with a power law of exponent of $\alpha = -1.50$. Finally, they calculated Ω_{CIV} ,

finding a value roughly 3 times higher than at $z \sim 5$, showing that the cosmic mass density of C IV has slowly but steadily increases from $z = 5$ to $z = 0$.

? measured the intergalactic C IV mass density at $4.3 < z < 6.3$ using the Magellan Folded-Port Infrared Echellette (FIRE) spectrograph. They confirmed the downturn in Ω_{CIV} at $z > 4$. They postulated that, due to the short physical timescale at these redshifts, this downturn may be driven primarily by ionization conditions. However, they cautioned that low number statistics still pose problems due to the limited number of sightlines to high redshift quasars.

Cooksey et al. (2013) used the Sloan Digital Sky Survey (SDSS) Data-Release 7 (DR7) to survey over 16,000 C IV systems with $1.46 < z < 4.55$ and rest frame equivalent widths ($W_r^{\lambda 1548}$) greater than 0.3 \AA . They found that the equivalent width frequency distribution ($f(W_r)$) was well-modeled by an exponential, with little evolution in its shape. In addition, they found dN/dX increased smoothly with decreasing redshift from $z = 4.55$ to $z = 1.96$ before plateauing at redshifts below 1.96. Their results suggest a monotonic increase in the amount of C IV enriched gas outside galaxies over the history of the universe.

? used *HST*/COS spectra of background quasars to measure elemental abundances in the low redshift intergalactic medium. They found that C IV has increased in abundance by a factor of 10 from $z \sim 5$ to present.

Bordoloi et al. (2014) measured C IV absorption in the COS-Dwarfs survey, probing the gaseous halos near 43 low-mass galaxies at $z \geq 0.1$. They detected C IV out to $\sim 100 \text{ kpc}$, roughly $0.5 R_{\text{vir}}$, from the host galaxies. They also reported a tentative correlation between C IV equivalent width and SFR, and concluded that energy-driven star formation winds must expel into the CGM a comparable mass to that of the carbon found in the stars of these galaxies.

? conducted a blind search of 89 quasar sightlines observed with the *HST* Cosmic Origins Spectrograph (COS) for low redshift C IV absorption. They identified 42 absorbers with $z < 0.16$. They determined that the number density of C IV absorbers per comoving path length and cosmic mass density relative to the critical density both increase marginally from $z \sim 1.5$ to present, confirming both extrapolated trends from higher redshifts and predictions from cosmological hydrodynamic simulations.

We begin by explaining the methods of acquiring and analyzing the quasar spectra in section 2. Next, in section 3, we present the results showing the evolution of the C IV equivalent width distribution, dN/dX , and the C IV column density distribution across redshift. In

section 4 we analyze the functional fit to the column density distribution and derive the relative matter density contributed to the universe by CIV, Ω_{CIV} . We also compare CIV to MgII in hopes of uncovering any global trends with metals in galaxy halos across redshifts spanning $0.1 < z < 5$. In Section 5 we summarize our results and look to future studies using this rich data set, including a companion analysis of intervening CIV absorbers and detailed kinematic analysis of intervening absorbing systems. For all calculations, we adopt the most recently published Planck cosmology, with $H_0 = 67.74 \text{ km s}^{-1} \text{ Mpc}$, $\Omega_M = 0.258$, and $\Omega_\Lambda = 0.742$.

2. DATA AND ANALYSIS

2.1. Quasar Spectra Sample

We have assembled a sample of **MANY** archival quasar spectra, representing **LESS MANY** unique sightlines, observed with the VLT/UVES and Keck/HIRES spectrographs. The data originate from three archival data mining efforts - the UVES SQUAD collaboration (432 spectra) led by Michael Murphy, the KODIAQ Survey (170 spectra) led by John O'Meara (O'Meara et al. 2015), and the work of ? which uses observations both from VLT/UVES and Keck/HIRES. The spectra range in signal-to-noise ratio (S/N) from 4 to 288 per $1.3 - 2.5 \text{ km s}^{-1}$ pixel, with the pixel size dependent upon the resolution of the spectrum. The mean S/N for the sample is 38 per pixel. Quasar emission redshifts span $0.014 < z < 5.292$. Wavelength coverage for each spectrum varies based upon the settings used for each spectrograph. VLT/UVES has 3 CCD chips available, offering large wavelength coverage from ~ 3000 to $\sim 10000 \text{ \AA}$. However, wavelength coverage available for each quasar spectrum varies based upon the selected cross-disperser settings. The exposures used from Keck/HIRES KODIAQ sample were taken from 2004 to present, when a 3 chip CCD mosaic was installed, also allowing wavelength coverage from ~ 3000 to $\sim 10000 \text{ \AA}$. Again, though, individual quasar observations vary in wavelength coverage based upon cross-disperser angle. The data from ? include **SOMETHING FROM VLT** and older Keck/HIRES observations, prior to the installation of the 3 chip mosaic, and reduced according to the prescriptions found in **CITE SOMETHING OF CHRIS'S HERE**. We detect **MANY** CIV absorbing systems from **redshift range** to a detection limit of $W_r^{\lambda 1548} \simeq 0.01 \text{ \AA}$ for regions with $S/N > 40$ per pixel.

2.2. Data Reduction and Line Detection

The KODIAQ data sample is reduced and fully continuum fit, delivered as normalized spectra according to the prescriptions of O'Meara et al. (2015). To summarize, observing runs are grouped together and uniformly reduced using HIREDUX¹ as part of the XIDL² suite of astronomical routines in IDL. Continuum fits are applied one order at a time using Legendre polynomials by a single member of the KODIAQ team, John O'Meara, to minimize bias and variation.

The UVES SQUAD sample also comes reduced and continuum fit according to the prescriptions of King et al. (2012); Bagdonaite et al. (2014); Murphy et al. (2016); Murphy (in prep). Reduction was carried out using the ESO Common Pipeline Language data-reduction software.³ The continuum is fit automatically with a low order polynomial in small sections using UVES_popler, an ESO/VLT UVES post-pipeline echelle reduction program written by Michael T. Murphy (Murphy 2016). This fit can incorrectly estimate the continuum around narrow emission regions and broad absorption features. Using UVES_popler, we add a higher order continuum fit to such regions of each spectrum, always preserving the continuity of the continuum with non-absorbing regions.

The ? sample combines data from both VLT/UVES and Keck/HIRES observations. As it is used in this paper, it also comes reduced and continuum fit according to the methods found in **DO I JUST CITE THE PHD HERE AGAIN?**.

The next step involves detecting all CIV absorption features. We first limit the search range to regions of the spectrum redward of the Ly α emission, as Ly α forest contamination would render automatic detection of weaker metal lines nearly impossible. We also do not search 5000 km s^{-1} blueward of the quasar emission redshift in order to avoid absorbers associated with the quasar itself. Finally, we exclude regions of strong telluric absorption bands, specifically from $6277 - 6318 \text{ \AA}$, $6868 - 6932 \text{ \AA}$, $7594 - 7700 \text{ \AA}$, and $9300 - 9630 \text{ \AA}$, because we found that the molecular line separations and ratios can lead to numerous false positives when searching for CIV doublets.

To find all intervening CIV $\lambda\lambda 1548, 1550$ absorbers, we employ a technique outlined in Zhu & Ménard (2013), in which we perform a matched filter search for absorption candidates detected above a certain S/N threshold. The filter is a top hat function centered at the wavelength of the desired redshifted absorption line. Its width is se-

¹ <http://www.ucolick.org/~xavier/HIREDUX/>

² <http://www.ucolick.org/~xavier/IDL/index.html>

³ http://www.eso.org/observing/dfo/quality/UVES/pipeline/pipe_reduc.htm

lected to match the resolution of the spectrum, which is a function of the slit width used during the exposure. A large variety of slit-widths were used to achieve different resolutions for varying science drivers, but, characteristically for a 1.0 arcsec slit, $R \sim 40,000$ for VLT/UVES and $R \sim 45,000$ for Keck/HIRES. We convolve the filter with the normalized spectrum to generate a normalized power spectrum in redshift space, with absorption features having positive power.

The error spectrum in both instruments is complex, irregular, and has frequent single-pixel spikes which makes uniform normalization impossible. Therefore, we cannot convolve the filter with the error spectrum to derive normalized noise estimates, as is often done in matched filter analysis. Instead, we examine the noise in the derived power spectrum.

To derive the noise, we first divide the power spectrum into smaller chunks which correspond to roughly 3000 pixels in the observed spectrum. We then sigma-clip these chunks to remove absorption features, leaving only the continuum power spectrum. Next, we calculate the standard deviation of this continuum. Finally, we use the standard deviation as the noise to calculate the S/N of the absorption features in the power spectrum as the ratio of the normalized power (S) to the normalized noise (N).

A flagged absorption feature has $S/N > 5$. A confirmed doublet detection for CIV $\lambda\lambda 1548, 1550$ requires detection of $S/N^{\lambda 1548} > 5$ and $S/N^{\lambda 1551} > 3$. In addition, our automated routines remove detections with non-physical doublet ratios in unsaturated regions; specifically, we exclude cases where $W_r^{\lambda 1551} > W_r^{\lambda 1548}$, or $W_r^{\lambda 1551} < (0.3 \times W_r^{\lambda 1548})$. The latter constraint is conservative for unsaturated CIV absorbers, as $W_r^{\lambda 1551}$ is rarely observed less than $0.5 \times W_r^{\lambda 1548}$. We relax this constraint in saturated features. This system could potentially exclude detections where either the CIV1548 or CIV1551 line is blended with another transition but does not saturate; however, confirmation of these cases requires extra verification from separate absorbing features, such as SiIV, which are weaker and not always covered in the spectrum.

All absorption features are visually verified upon completion of the detection algorithm. Multiple feature detections within $\pm 500 \text{ km s}^{-1}$ of each other are grouped together to generate absorption systems, designated as a single absorber, to be analyzed. Once absorption systems are identified, we calculate the optical depth-weighted median absorption redshift to define the center of the entire absorption system. The formal derivation of this redshift is described in the appendix of Churchill & Vogt (2001).

We also derive an equivalent width detection limit across the spectrum. To do so, we insert modeled Gaussian absorption features across the spectrum and assume a full-width at half maximum (FWHM) defined by the resolution of the instrument to represent unresolved lines. We then solve for the height of the Gaussian, defined as the value at the curve's peak, required to detect the unresolved line with our matched filtering technique at a $S/N = 5$. Finally, we integrate to find the equivalent width, and take that value as the minimum detectable equivalent width at a given wavelength. The detection algorithm is therefore self-monitoring. This full equivalent width detection limit spectrum also allows us to accurately characterize the completeness of our sample, along with the full redshift path length searched.

2.3. Measuring Absorption Properties

For each absorption system, we automatically define the wavelength bounds of an absorbing region by finding where the flux recovers to within 1σ of the continuum, with σ defined by the error spectrum, for three pixels on either side of the absorption trough. Within these regions we calculate rest-frame equivalent widths (W_r), velocity widths (Δv), optical depth-weighted kinematic spreads (ω_v), and apparent optical depth (AOD) column densities ($\log(N)$). The functional forms of these parameters are detailed in the appendix of Churchill & Vogt (2001), equations A3 – A7. In the case of saturated lines, where the absorption profile reaches zero flux, the AOD column density calculation represents only a lower limit. In such cases, we adopt the column density value derived from the CIV1551 profile.

3. RESULTS

3.1. Sample Characterization

Figure 1 shows the relationships between the measured absorption parameters, characterizing the distribution of absorption properties for our survey. We cover a large parameter space, examining all types of observable absorption systems from $SOMETHING < W_r^{\lambda 1548} < 5 \text{ \AA}$

3.2. Sample Completeness and Survey Path Coverage

Figure 2 shows the function $g(W_r^{\lambda 1548}, z)$. This 2D heat map details the number of spectra in which a CIV $\lambda\lambda 1548, 1550$ doublet could be detected as a function of the equivalent width detection limit and redshift. The vertical stripes with no redshift path coverage represent the omitted telluric absorption regions for our survey. The integral along a given $W_r^{\lambda 1548}$ slice gives the total redshift path length available for the sample.

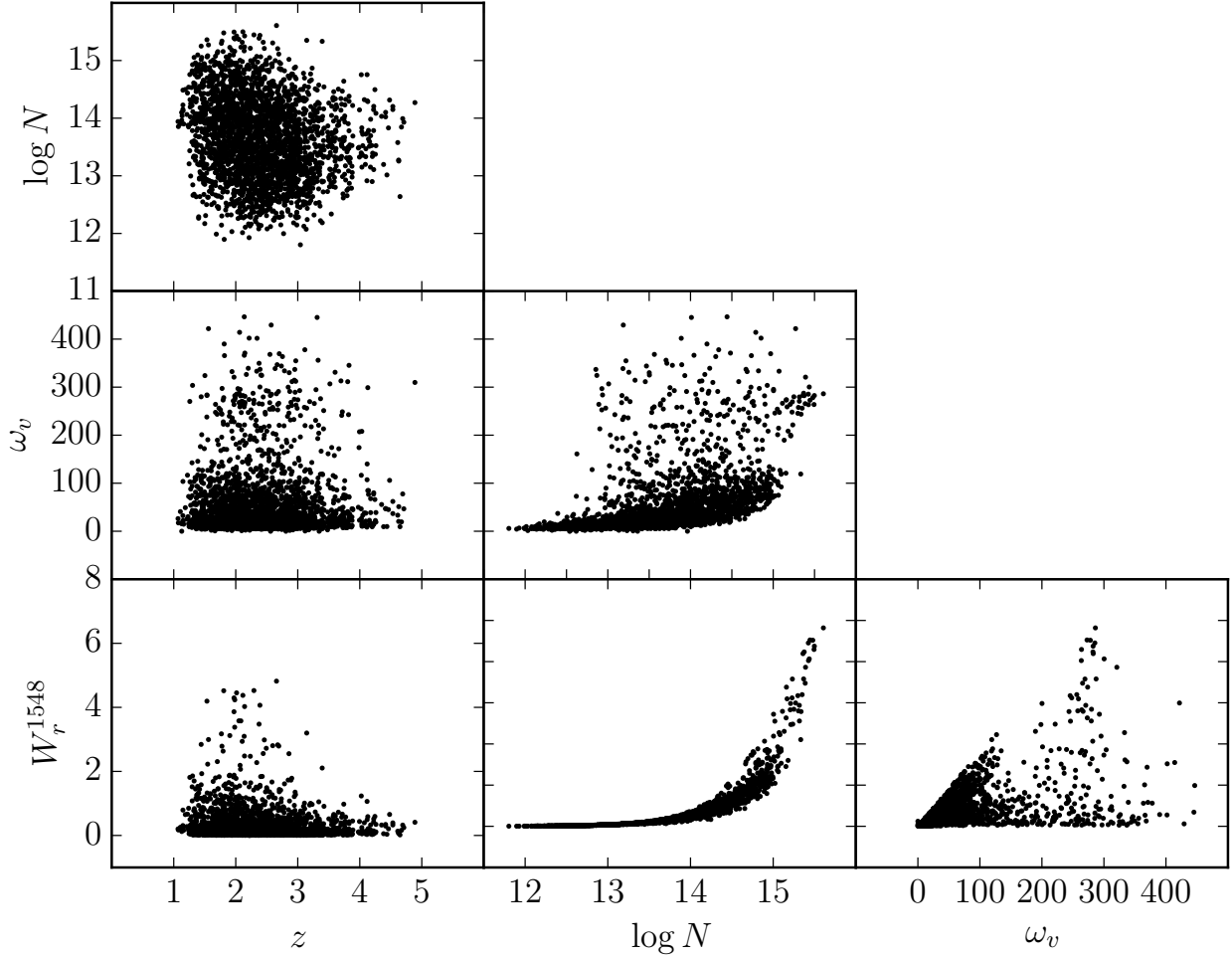


Figure 1. Correlations between measured absorption properties for survey sample. $\log N$ is the AOD column density, ω_v is the kinematic spread, W_r^{1548} is the rest frame CIV1548 equivalent width, and z is the absorption redshift.

3.3. dN/dZ and dN/dX

Previous studies of the statistical properties of CIV absorbers have thoroughly characterized CIV absorbers with equivalent widths above $W_r^{1548} = 0.3 \text{ \AA}$. This corresponds to the detection limit of the Sloan Digital Sky Survey (SDSS), which catalogs hundreds of thousands of quasar spectra. Unfortunately, the distribution of the low equivalent width regime of CIV absorbers has not been characterized.

We follow the prescriptions of Paper 1, in which we details the calculations of dN/dz and dN/dX , the redshift path density and absorption path density, respectively. These metrics describe the expected number of detected absorbers through a given redshift or absorption path length.

In Figures 3 and 4, we plot dN/dz and dN/dX as a function of redshift for varying equivalent width cuts. Dotted lines are fit according to the analytical form which allows for redshift evolution in dN/dX , defined as,

$$\frac{dN}{d(z, X)} = n\sigma(1+z)^\epsilon, \quad (1)$$

where n is the number density of CIV absorbers, σ is the absorbing cross-section, and ϵ is the power dependence of dN/dX on redshift.

In Figures 5 and 6, we show the evolution of the Hubble opacity and the evolution parameter as a function of different equivalent width cuts. As we apply larger equivalent width cuts, $n\sigma$ stays relatively flat before rising to a peak at $W_r^{1548} = 0.7 \text{ \AA}$. This value then drops precipitously, representing a decreasing inci-

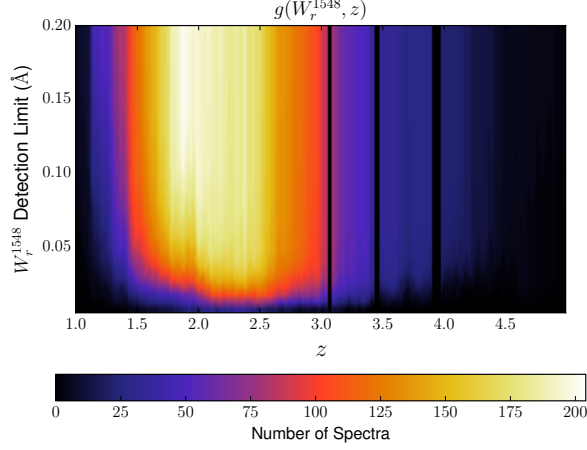


Figure 2. The function $g(W_r^{1548}, z)$ shown as 2D heat map with the colors representing the value of $g(W_r^{1548}, z)$. This is the number of spectra in which an absorption line of a given equivalent width and a given redshift may be detected according to the detection limit of the spectrum. The vertical black bars representing no redshift path length coverage show the omitted wavelength regions of the survey based upon contaminating telluric absorption features.

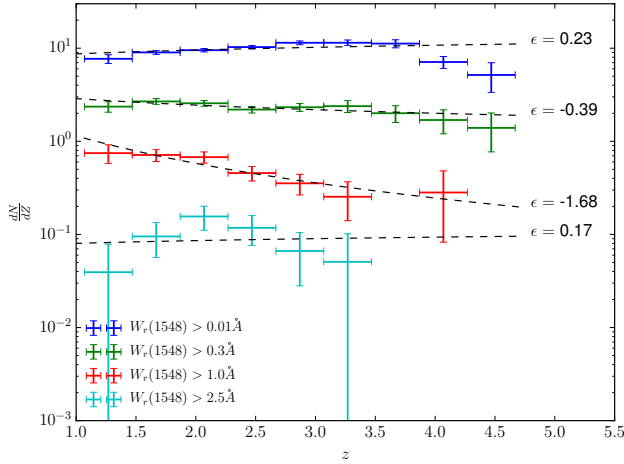


Figure 3. $\frac{dN}{dz}$ as a function of redshift for varying $W_r^{\lambda 1548}$ cuts. Colors represent different equivalent width cuts. The black dotted lines are fits to the distribution of the functional form $f(z) = n\sigma(1+z)^\epsilon$, with the best fit ϵ value labelled.

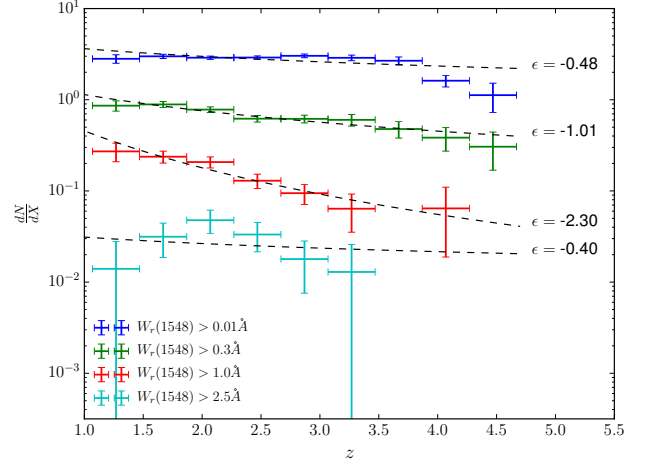


Figure 4. $\frac{dN}{dX}$ as a function of redshift for varying $W_r^{\lambda 1548}$ cuts. Colors represent different equivalent width cuts. The black dotted lines are fits to the distribution of the functional form $f(z) = n\sigma(1+z)^\epsilon$, with the best fit ϵ value labelled. We see increasing values of ϵ with increasing equivalent width, driven by an enhancement of stronger CIV absorbers around redshift 2 compared to lower redshifts.

changes, but instead because the distribution takes on a different shape not well described by Equation 1, where dN/dz and dN/dX peak around $z = 2$, but decrease towards higher and lower redshifts.

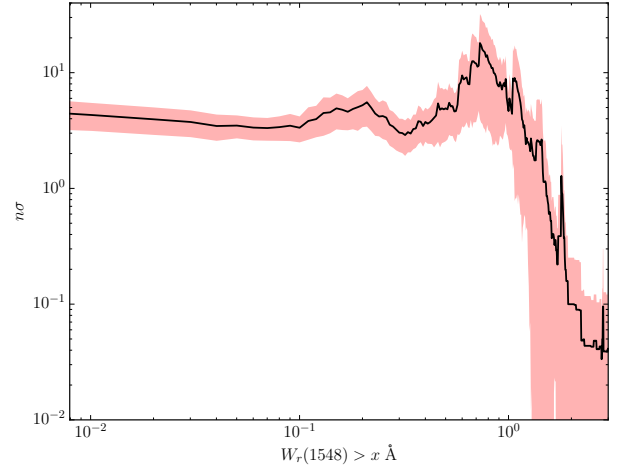


Figure 5. Absorber space density times cross section, as derived from the functional fit $dN/dX = n\sigma(1+z)^\epsilon$ as a function of cumulative equivalent width cut, where $W_r^{\lambda 1548} > x$ Å. As CIV equivalent width increases, either the space density of absorbing cloud structures decreases, the absorbing cross-section decreases, or both parameters decrease.

dence of very strong CIV absorbers, whether by decreasing number density, absorbing cross-section, or both. In addition, ϵ becomes more negative with increasing equivalent width cuts up until around $W_r^{\lambda 1548} = 0.7$ Å, at which point it rises again for the strongest CIV absorbers. This transition at $W_r^{\lambda 1548} = 0.7$ Å occurs not because the overall slope of the distribution necessarily

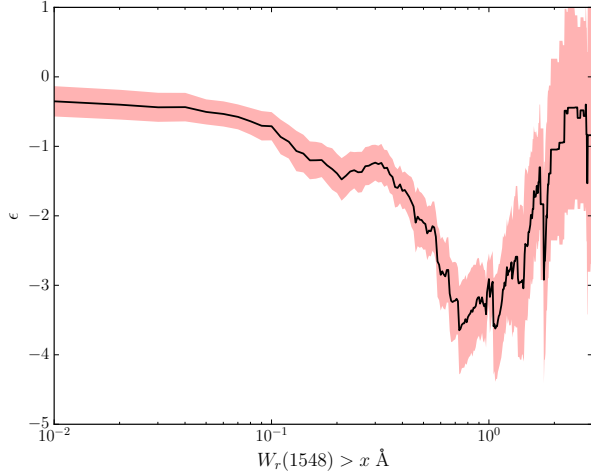


Figure 6. Redshift power dependence of the functional fit $dN/dX = n\sigma(1+z)^\epsilon$ as a function of cumulative equivalent width cut, where $W_r^{\lambda 1548} > x \text{ \AA}$. Weak CIV absorbers are more abundant at low redshift, leading to a negative coefficient ϵ . Moderate equivalent width CIV absorbers do not evolve, showing $\epsilon \simeq 0$. Strong CIV absorbers evolve away at low redshift, showing a large positive ϵ increasing towards $z = 2$.

3.4. Equivalent Width Frequency Distribution

We calculate the equivalent width frequency distribution by first calculating dN/dz and dN/dX for each absorber equivalent width, then summing the distribution in equivalent width bins, and then dividing by the bin width. We examine four redshift bins, requiring that the number of absorbers in each redshift range remains constant.

In Figure 8, we plot the equivalent width frequency distribution. We fit this distribution with a Schechter function to parameterize the distribution and to compare the relative differences between varying redshift cuts. We find the low equivalent width slope decreases towards shallower values as redshift increases, implying a decrease in weak CIV absorbers and a relative increase in strong CIV absorbers from low redshift to redshifts near $z = 2$.

3.5. Column Density Distribution

To calculate the column density distribution, we calculate dN/dX for each absorber equivalent width, sum the distribution in column density bins, and then divide by the bin width. The result is a characteristic number density of CIV absorbers per absorption path length as a function of their column densities. It should be noted that at high column densities near $\log(N(\text{CIV})) = 15$, the measured column densities are lower limits as the

AOD method to measure column densities cannot constrain the true column when the line saturates.

In Figure 10, we plot the column density frequency distribution. Again, we fit this distribution with a Schechter function. We find again that the low column density end of the distribution becomes shallower as one goes from low redshift to $z = 2$. Due to saturation effects, the final high column density bin is likely best regarded as a lower limit.

3.6. Comparison with MgII Absorption Properties

Comparison plots and comparison table of evolution of Schechter fits and evolution of dN/dX plotted on the same axis.

4. DISCUSSION

4.1. Evolution of CIV Distributions

Discuss all previous CIV surveys in order.

Discuss Jane's interpretation of changing ionizing background in order to link the CIV and MgII properties.

4.2. Ω_{CIV}

We now aim to calculate the matter density of CIV absorbers across cosmic time using the following equation,

$$\Omega_{\text{CIV}} = \frac{H_0 m_{\text{Mg}}}{c \rho_{c,0}} \int_{N_{\min}}^{N_{\max}} f(N_{\text{CIV}}) N_{\text{CIV}} dN_{\text{CIV}}, \quad (2)$$

where H_0 is the Hubble constant today, $m_{\text{Mg}} = 4.035 \times 10^{-23} \text{ g}$, c is the speed of light, $\rho_{c,0}$ is the critical density at present, $f(N_{\text{CIV}})$ is the column density distribution of CIV absorbers, and N_{CIV} is the column density. We numerically integrate the Schechter Function fit to $f(N_{\text{CIV}})$, multiplied by N_{CIV} . The results are shown below in Figure 11.

Errors are derived by bootstrap Monte-Carlo, performing the same sample analysis outlined in Sections 3.5 and 4.2 on a random sample, selected with replacement, of CIV absorbers. We take the standard deviation about the mean of this ensemble of random samples as the error in Ω_{CIV} .

4.3. Potential Causes for Trends

The most obvious conclusion to be drawn from our CIV survey is that around redshift $z = 2$, something changes in the distribution of CIV absorbers. The number of strong absorbers per unit path length increases, the faint end slope of the equivalent width and column density distributions flattens, the 'knee' of the Schechter

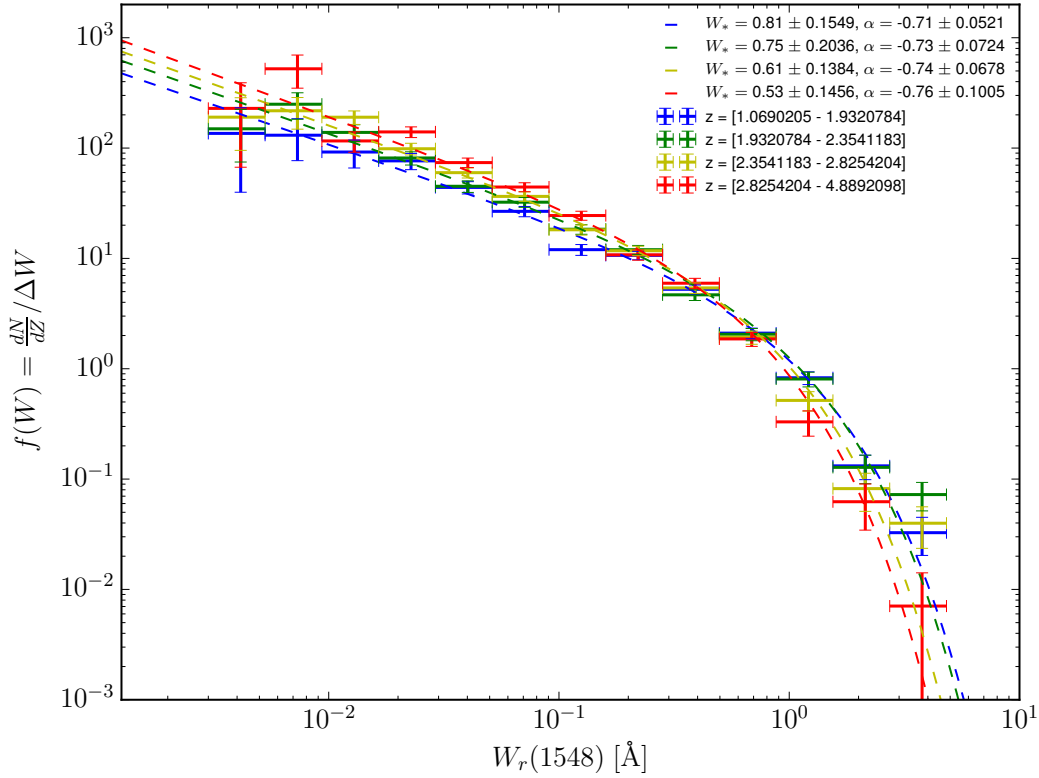


Figure 7. The equivalent width distribution of CIV absorbers, defined as the comoving line density ($\frac{dN}{dZ}$) in each equivalent width bin divided by the bin width. We fit this distribution with a Schechter function, capturing the self-similar power law behavior of the distribution before the exponential cutoff limiting the size of CIV absorbers.

fit of the equivalent width and column density distributions pushes outward to higher $W_r^{\lambda 1548}$ and $N(\text{CIV})$, and the cosmic mass density of CIV increases. We can now state that the physical properties driving the global distribution of CIV absorbers changes around $z = 2$. Possible explanations relate to the ionization conditions in the halos of galaxies at this time, the metallicity of gas around galaxies, or the quantity of metals in the circumgalactic medium.

Haardt & Madau (2012) represents the most recent and robust estimate of the cosmic ionizing background as a function of redshift, which is the primary ionizing component responsible for the global ionization state of gas in galactic halos. REDSHIFT EVOLUTION OF BACKGROUND RADIATION. DISCUSS HOW THIS DOES NOT PRODUCE TRENDS.

The metallicity of galaxy halos as a whole is not well characterized over time. However, if we assume that the metals in galaxy halos are built up as a result of outflows (Quijet et al. 2016), and that the metallicity of the halo may scale with the metallicity of the ISM, then it would make no sense to observe larger quan-

ties of CIV in the circumgalactic medium at $z = 2$ compared to HIGHER REDSHIFTS. DISCUSS HOW THIS DOES/DOES NOT SUPPORT THE TRENDS WE OBSERVE.

5. CONCLUSIONS

Using archival data from *VLT/UVES* and *KECK/HIRES*, we have undertaken the most complete survey of CIV absorbers in 602 quasar spectra in high resolution ($\sim 7 \text{ km s}^{-1}$) allowing for the detection of both strong and weak CIV absorbers. Our survey spans absorption redshifts from $0.18 < z < 2.57$, allowing for characterization of the evolution of the distribution of these absorbers across cosmic time. Using our own detection and analysis software, we are able to accurately characterize the equivalent width detection limit, absorption path length, and survey completeness to a level allowing for an accurate determination of dN/dZ , the equivalent width distribution function, the column density distribution function, and the total cosmic mass density of CIV absorbers. Our main findings are as follows:

1. Stuff

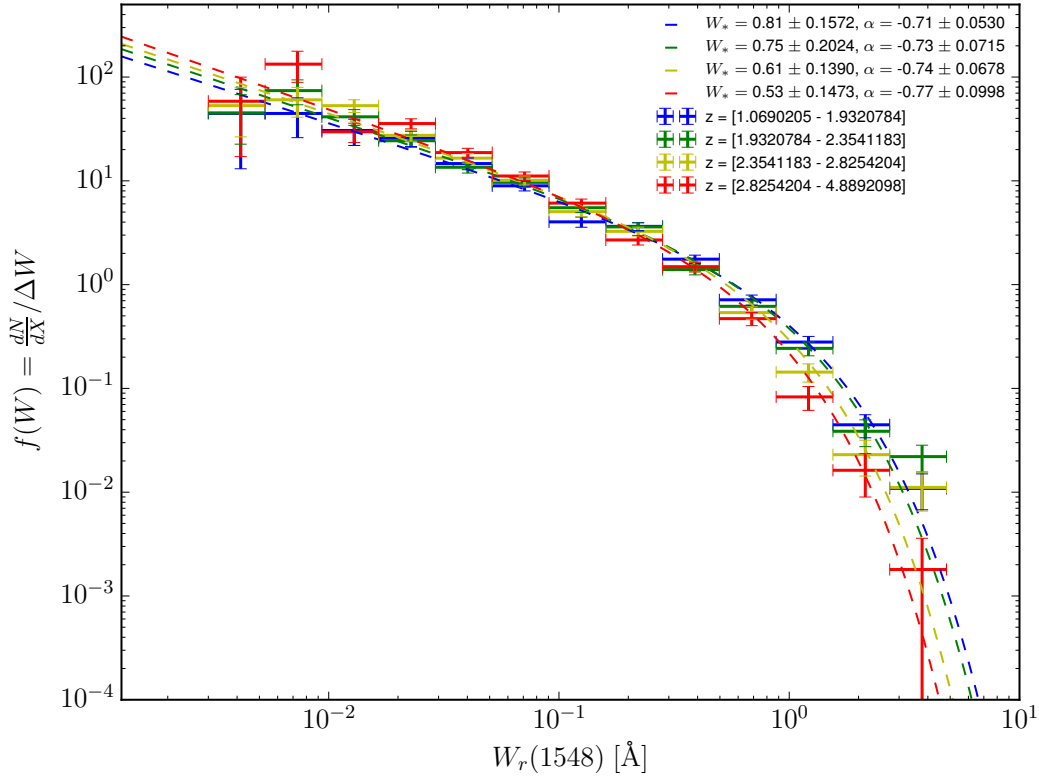


Figure 8. The equivalent width distribution of C IV absorbers, defined as the comoving line density ($\frac{dN}{dX}$) in each equivalent width bin divided by the bin width. We fit this distribution with a Schechter function, capturing the self-similar power law behavior of the distribution before the exponential cutoff limiting the size of C IV absorbers.

2. Things

3. more stuff and things

M.T.M. thanks the Australian Research Council for
Discovery Project grant DP130100568 which supported

this work. C.W.C. thanks the National Science Founda-
 tion for the grant AST-1517816, which partially sup-
 ported this work.

REFERENCES

- Bagdonaite, J., Ubachs, W., Murphy, M. T., & Whitmore, J. B. 2014, *ApJ*, 782, 10
- Bordoloi, R., Lilly, S. J., Kacprzak, G. G., & Churchill, C. W. 2014, *ApJ*, 784, 108
- Chen, H.-W., Lanzetta, K. M., Webb, J. K., & Barcons, X. 2001, *ApJ*, 559, 654
- Churchill, C. W., Rigby, J. R., Charlton, J. C., & Vogt, S. S. 1999, *ApJS*, 120, 51
- Churchill, C. W., & Vogt, S. S. 2001, *AJ*, 122, 679
- Cooksey, K. L., Kao, M. M., Simcoe, R. A., O’Meara, J. M., & Prochaska, J. X. 2013, *ApJ*, 763, 37
- Haardt, F., & Madau, P. 2012, *ApJ*, 746, 125
- King, J. A., Webb, J. K., Murphy, M. T., et al. 2012, *MNRAS*, 422, 3370
- Murphy, M. T. 2016, UVES-popler: POst PipeLine Echelle Reduction software, doi:10.5281/zenodo.44765
- . in prep, *MNRAS*
- Murphy, M. T., Malec, A. L., & Prochaska, J. X. 2016, *MNRAS*, 461, 2461
- O’Meara, J. M., Lehner, N., Howk, J. C., et al. 2015, *AJ*, 150, 111
- Quiret, S., Péroux, C., Zafar, T., et al. 2016, *MNRAS*
- Zhu, G., & Ménard, B. 2013, *ApJ*, 770, 130

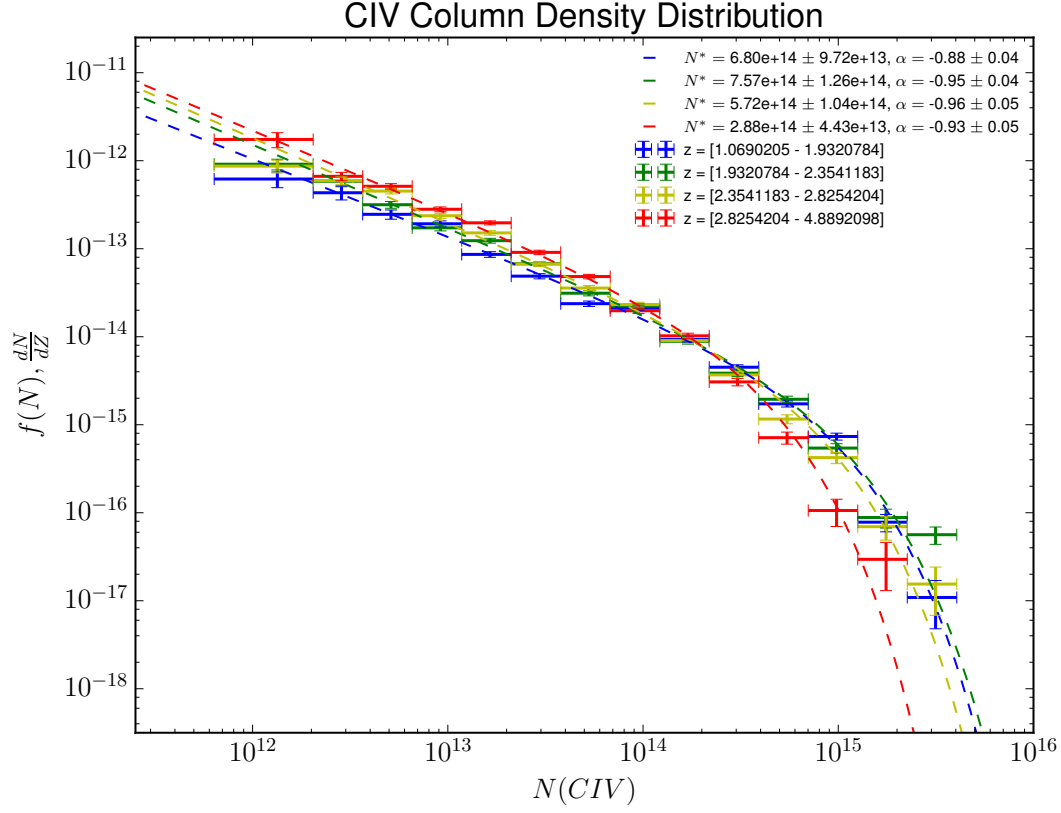


Figure 9. The column density distribution of CIV absorbers, defined as the comoving line density in each column density bin divided by the bin width. We fit this distribution with a Schechter function.

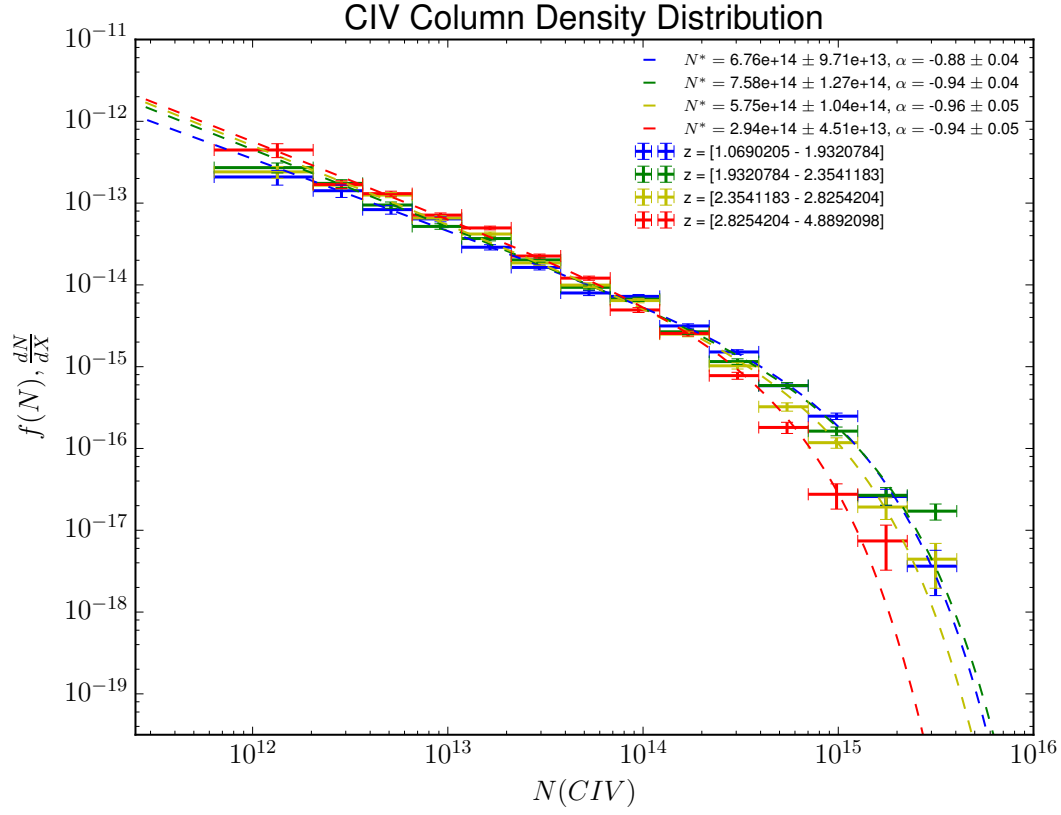


Figure 10. The column density distribution of CIV absorbers, defined as the comoving line density in each column density bin divided by the bin width. We fit this distribution with a Schechter function.

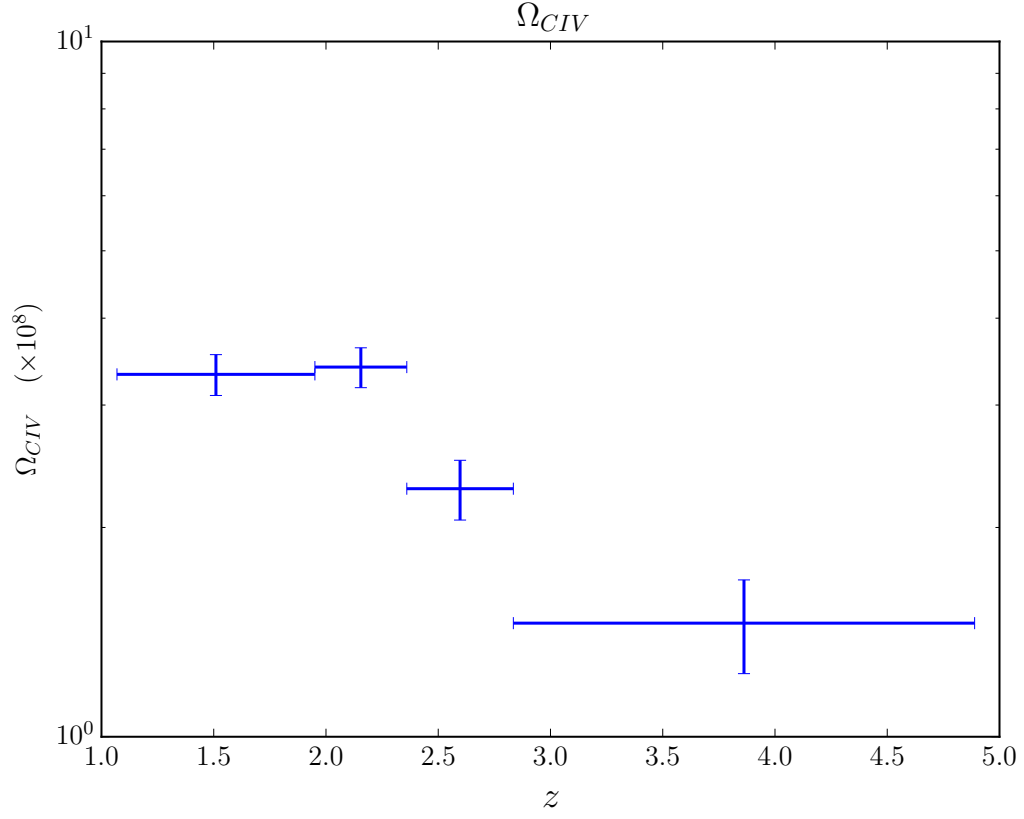


Figure 11. Ω_{CIV} as a function of redshift. The cosmic mass density of CIV stays roughly flat near a value of 1×10^{-9} , with a potential increase from $z = 0.1$ to $z = 2.5$.